Atmospheric Environment 44 (2010) 2415–2426

Contents lists available at ScienceDirect

Atmospheric Environment

journal homepage: www.elsevier.com/locate/atmosenv

Understanding of regional air pollution over China using CMAQ, part I performance evaluation and seasonal variation

Xiao-Huan Liu [a,b], Yang Zhang [b,*], Shu-Hui Cheng [a,b], Jia Xing [c], Qiang Zhang [d], David G. Streets [d], Carey Jang [e], Wen-Xing Wang [a], Ji-Ming Hao [c]

[a] Shandong University, Jinan, Shandong Province 250100, PR China
[b] North Carolina State University, Raleigh, NC 27695, USA
[c] Tsinghua University, Beijing 100084, PR China
[d] Argonne National Laboratory, Argonne, IL 60439, USA
[e] The U.S. Environmental Protection Agency, Research Triangle Park, NC 27711, USA

ARTICLE INFO

Article history:
Received 10 December 2009
Received in revised form
26 March 2010
Accepted 29 March 2010

Keywords:
CMAQ
Model evaluation
Seasonality
China
Sensitivity to horizontal grid resolution

ABSTRACT

The U.S. EPA Models-3 Community Multiscale Air Quality (CMAQ) modeling system with the process analysis tool is applied to China to study the seasonal variations and formation mechanisms of major air pollutants. Simulations show distinct seasonal variations, with higher surface concentrations of sulfur dioxide (SO_2), nitrogen dioxide (NO_2), and particulate matter with aerodynamic diameter less than or equal to 10 μm (PM_{10}), column mass of carbon monoxide (CO) and NO_2, and aerosol optical depth (AOD) in winter and fall than other seasons, and higher 1-h O_3 and troposphere ozone residual (TOR) in spring and summer than other seasons. Higher concentrations of most species occur over the eastern China, where the air pollutant emissions are the highest in China. Compared with surface observations, the simulated SO_2, NO_2, and PM_{10} concentrations are underpredicted throughout the year with NMBs of up to −51.8%, −32.0%, and −54.2%, respectively. Such large discrepancies can be attributed to the uncertainties in emissions, simulated meteorology, and deviation of observations based on air pollution index. Max. 1-h O_3 concentrations in Jan. and Jul. at 36-km are overpredicted with NMBs of 12.0% and 19.3% and agree well in Apr. and Oct. Simulated column variables can capture the high concentrations over the eastern China and low values in the central and western China. Underpredictions occur over the northeastern China for column CO in Apr., TOR in Jul., and AODs in both Apr. and Jul.; and overpredictions occur over the eastern China for column CO in Oct., NO_2 in Jan. and Oct., and AODs in Jan. and Oct. The simulations at 12-km show a finer structure in simulated concentrations than that at 36-km over higher polluted areas, but do not always give better performance than 36-km. Surface concentrations are more sensitive to grid resolution than column variables except for column NO_2, with higher sensitivity over mountain and coastal areas than other regions.

1. Introduction

During the past 30-year, China experienced a rapid economic development and industrial expansion, with a significant increase in anthropogenic emissions, especially over the eastern China, one of the regions with the highest emissions in the world and an increased exposure to ozone (O_3) and particulate matter with aerodynamic diameter less than and equal to 10 μm (PM_{10}). Hao et al. (2007) reported that among 522 cities with air quality monitoring sites, only 22 cities (or 4.2%) met the Class I of the National Ambient Air Quality Standard of China that was set to protect natural environments, 293 (or 56.1%) met the Class II standard that was set to protect humans and sensitive plants in urban residential, commercial/residential, cultural, or rural areas, and the remaining cities are in non-attainment and severely polluted.

A number of modeling studies have been recently conducted at a regional scale over East Asia or China. Tie et al. (2006) reported that rates of O_3 production and O_3 concentrations during summer in the eastern China were significantly lower than those in the

* Corresponding author. Department of Marine, Earth, and Atmospheric Sciences, Campus Box 8208, NCSU, Raleigh, NC 27606, USA. Tel.: +1 919 515 9688; fax: +1 919 515 7802.
E-mail address: yang_zhang@ncsu.edu (Y. Zhang).

1352-2310/$ – see front matter © 2010 Elsevier Ltd. All rights reserved.
doi:10.1016/j.atmosenv.2010.03.035

eastern U.S., because of considerably lower volatile organic compounds (VOCs). Yamaji et al. (2006) found that O_3 chemistry is NO_x-limited during summer time over East Asia. Liu et al. (2007) found that emissions of O_3 precursors and O_3 formation are the highest over the central and eastern China. Song et al. (2008) reported high aerosol optical depth (AOD) over Sichuan Basin, Bohai Bay, and the Yangtze River Delta (YRD) areas and AODs were underpredicted in spring due to the occurrence of dust storms and biomass plumes but overpredicted in other seasons due to overpredicted PM_{10} caused by overestimated NH_3 emissions. Using the Community Multiscale Air Quality (CMAQ), Wang et al. (2009) found that Asian pollution enhanced background concentrations of O_3 and SO_4^{2-} in the western U.S. by ~2.5% and ~20%, respectively.

Several modeling studies have also been performed at an urban scale over the Beijing area after its selection to be the host city for the 2008 Olympic Games. An et al. (2007) reported the contributions of non-Beijing sources of 39% to $PM_{2.5}$ and 30% to PM_{10} over the Beijing metropolitan area during a heavy air pollution episode 3–7 Apr. 2005. Streets et al. (2007) predicted that more than 30% of $PM_{2.5}$ and O_3 may be transported to the Olympic Stadium site from the sources outside Beijing during summer. Chen et al. (2007) also found that air quality improvement in Beijing requires emission reductions of sources outside of Beijing. Xu et al. (2008) found that the O_3 chemistry in the Beijing area was VOC-limited, which changed to NO_x-limited in its downwind areas during typical summer conditions.

The above studies focused largely on gas-phase air pollutants at the surface during a specific air pollution episode (mostly prior to 2005). None of them provide a comprehensive examination of the seasonality and formation mechanism of both O_3 and PM species over China. In this study, CMAQ is applied at 36-km over East Asia and a nested 12-km over the eastern China for Jan., Apr., Jul., and Oct. 2008 to study the seasonal variation and formation mechanisms of major pollutants such as O_3 and PM_{10}. Part I describes the model setup, evaluation datasets and protocols, simulated seasonal variations of major air pollutants and the results from model evaluation using surface and satellite observations. The sensitivity of model predictions to horizontal grid resolutions is also examined. Part II presents results from process analysis (PA) and additional sensitivity studies, identifies the most influential processes that lead to the formation and accumulation of major pollutants in China. The regime of O_3 chemistry and PM formation is diagnosed based on PA, then verified through sensitivity simulations. The policy implications of such regime analyses are discussed.

2. Model setup and evaluation protocols

CMAQ version 4.7 released in Dec. 2008 (Byun and Schere, 2006) is applied over East Asia for the 4-month simulations in 2008. Fig. S-1 in the Supplementary data shows the nested domains, with the 36-km domain over East Asia, and the 12-km domain over the eastern China. The vertical resolution includes 14 logarithmic structure layers from the surface to the tropopause, with the first model layer height of 36-m above the ground level. The meteorological fields are generated by the Pennsylvania State University/National Center for Atmospheric Research Mesoscale Modeling System Generation 5 (MM5) version 3.7 with four-dimensional data assimilation. The MM5 hourly output files are processed with the Meteorology-Chemistry Interface Processor version 3.0. More details about the meteorology simulation and evaluation can be found in Cheng et al. (in preparation). Emissions are generated by extrapolating the 2006 activity data to the year 2008 using the method described by Q. Zhang et al. (2009) and by updating those reported by Streets et al. (2006) and Zhang et al. (2007a, b). Initial conditions (ICONs) and boundary conditions (BCONs) are generated using the results from a global chemistry model of GEOS–CHEM. The 4-month simulations are performed separately, each with a 1-week spin-up period to minimize the influence of ICONs.

Table 1 summarizes the variables and observational data included in the model evaluation. The species include the surface concentrations of sulfur dioxide (SO_2), nitrogen dioxide (NO_2), and PM_{10} using observations derived from the Air Pollution Index (API) (http://www.zhb.gov.cn/quality/air.php3) in 23–24, 6–22, and 86 major cities, respectively, in China and hourly O_3 mixing ratios from Mt. Tai located in the eastern China and 3 sites (Ryori, Tsukuba, and Yonagunijima) in Japan. API is piecewise linearly related to the observed concentrations of SO_2, NO_2, and PM_{10}. The derived concentrations from API have been used for model evaluation (Jiang et al., 2004; Wang et al., 2009), despite some uncertainties. Satellite data are also used to evaluate column mass abundance of several species (i.e., carbon monoxide (CO), NO_2, tropospheric ozone residual (TOR)), and AODs to complement sparse surface data. Following the approach of Y. Zhang et al. (2009), the simulated total column mass of species and AODs are calculated using the 3-D gridded hourly average mixing ratios of CO, NO_2, O_3, and concentrations of $PM_{2.5}$ species predicted by CMAQ and vertically-resolved temperature and pressure estimated from MM5. Model evaluation is performed in terms of spatial distribution, temporal variation, column abundances, and overall domain-wide statistical trends using an evaluation protocol of Y. Zhang et al. (2009).

Table 1
Variables evaluated and observational data used in this study.

Datasets	Data type	Species	Data frequency	Number of sites	Data sources and notes
API	PM	PM_{10}	Daily	86	http://datacenter.mep.gov.cn/TestRunQian/air_dairy.jsp
API	Gas	SO_2, NO_2	Daily	Jan. NO_2: 6 Apr., Jul., Oct. NO_2: 22 Jan. SO_2: 23 Apr., Jul., Oct. SO_2: 24	Beijing: www.bjee.org.cn/api/; Shanghai: www.sepb.gov.cn/hjzhiliang/main.jsp; Guangzhou: www.gzepb.gov.cn/comm/apidate.asp; Guiyang: www.ghb.gov.cn/Gazette.asp; Wuhan: www.whepb.gov.cn/publish/whhbj/2008-07/17/kq/1200807171552400040.html; Xi'an: www.xianemc.gov.cn/airsearch.asp?tablename=airrb&;year1=2008 16 cities in Shandong: http://www.sdein.gov.cn/ Other sites: http://datacenter.mep.gov.cn/TestRunQian/air_dairy.jsp
WDCGG	GAS	O_3	Hourly	3	http://gaw.kishou.go.jp/cgi-bin/wdcgg/catalogue.cgi
Mt. Tai	GAS	O_3	Hourly	1	Shandong University, China; note that no observations were available at Mt. Tai in most days in Jan. and all days in Jul. 2008
OMI		Column NO_2, TOR	Monthly average	N/A	http://disc.sci.gsfc.nasa.gov/data/datapool/OMI http://hyperion.gsfc.nasa.gov/Dataservices/cloudslice
MODIS		AOD	Monthly average	N/A	http://ladsweb.nascom.nasa.gov/data/search.html
MOPITT		Column CO	Monthly average	N/A	http://eosweb.larc.nasa.gov/PRODOCS/mopitt/table_mopitt.html

API – Air Pollution Index; WDCGG – the World Data Center for Greenhouse Gases; OMI – the Ozone Monitoring Instrument; MODIS – the Moderate Resolution Imaging Spectroradiometer; MOPITT – the Measurements of Pollution in the Troposphere; TOR – tropospheric ozone residual, AOD – aerosol optical depth.

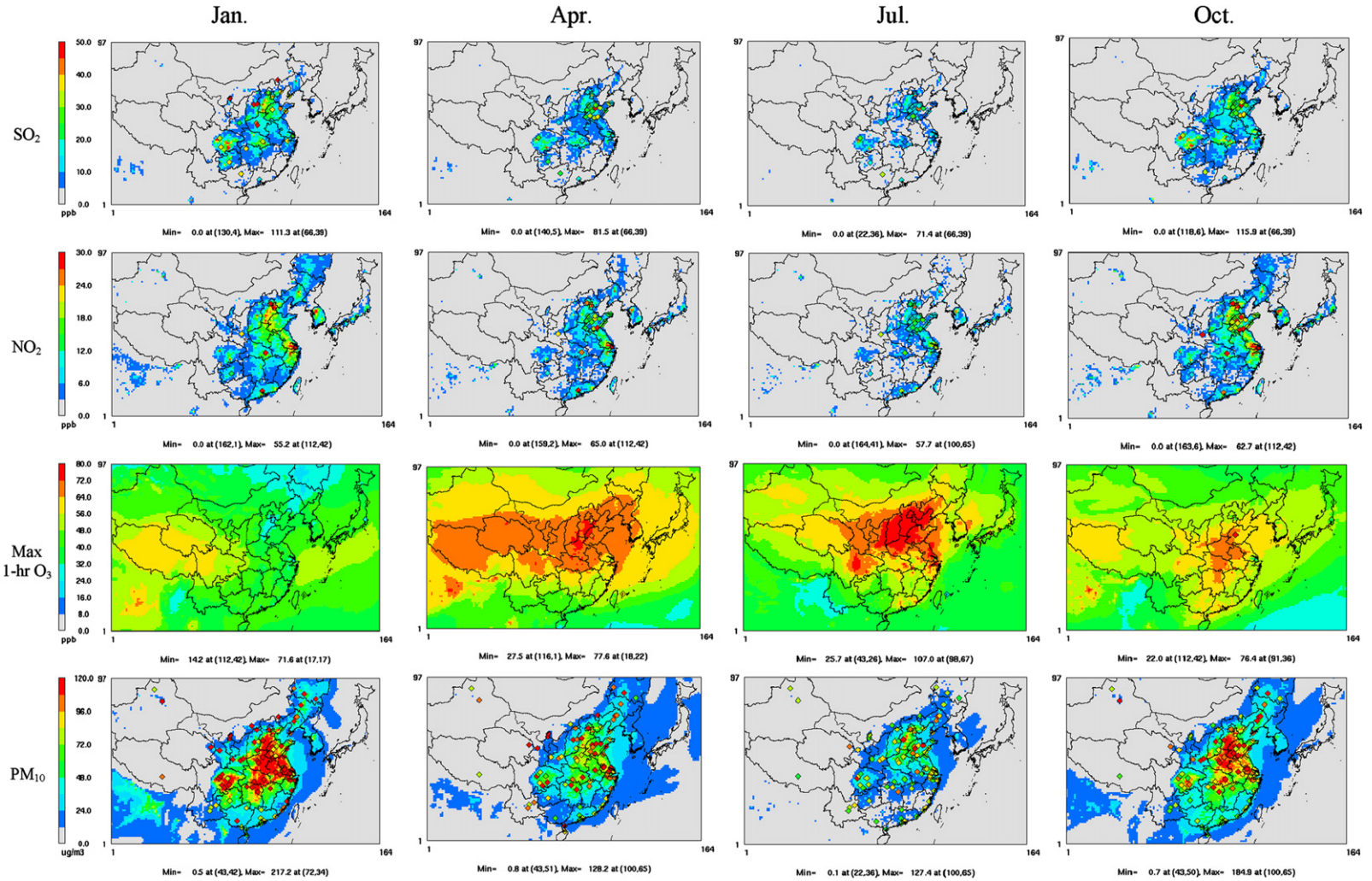

Fig. 1. Overlay of simulated and observed surface concentrations of 1-h max. O_3, PM_{10}, SO_2 and NO_2 in 2008 at a 36-km grid resolution. Diamond signs indicate the observations, including O_3 concentrations from Mt Tai, and 3 sites in Japan (note that no observations were available at Mt. Tai in Jan. and Jul.), PM_{10} concentrations are derived from the API data for 86 major cities in China, and the mixing ratios of SO_2 and NO_2 are derived from the API data for 6 cities in China: Beijing, Xi'an, Wuhan, Shanghai, Guangzhou, and Guiyang.

3. Model evaluation

3.1. Surface concentrations

3.1.1. Spatial distribution and performance statistics

Fig. 1 shows the observed vs. simulated spatial distributions of monthly-mean daily-average surface concentrations of SO_2 and NO_2, max. 1-h O_3, and daily-average PM_{10} at 36-km. The highest SO_2 concentration was simulated in Jan. in the eastern China, which is caused by the highest SO_2 emissions in winter resulted from an extensive coal combustion over the northern China, coupled with the low wind speed and dry weather conditions controlled by Siberian high in winter that are not conducive to dispersion and scavenging for pollutants. Low planetary boundary layer (PBL) height and temperature inversion in winter also prevent the dispersion of air pollutants. Emissions of SO_2 in other months are similar. The simulated SO_2 concentrations, however, in Oct. are higher than those in Apr. and Jul. due to several reasons. First, the weaker solar radiation in fall than in summer slows down the photochemical conversion from SO_2 to SO_4^{2-}. Second, the least amount of precipitation in fall among the four seasons as shown in Cheng et al. (in preparation) causes a slow wet scavenging and aqueous-phase oxidation rate of SO_2. In addition, higher wind speeds in Apr. than in Oct. would enhance the ventilation of SO_2. The lowest SO_2 levels are found in Jul., due to a strong solar radiation that favors its photochemical conversion and the heaviest precipitation among the four months that favors its aqueous-phase oxidation. Higher PBL height in Jul. also helps the dispersion of SO_2. In addition, the highest RHs and the highest NH_3 emissions in Jul. favor the formation of ammonium sulfate. These factors lead to the highest SO_4^{2-} concentration in Jul.

NO_2 concentrations show a similar seasonal variation trend to SO_2, with the maximum in Jan., followed by Oct., Apr., and Jul. The highest NO_2 concentrations in winter are resulted from the highest NO_2 emissions and the suppressed photochemical reaction rates and longer lifetime of NO_2. North China Plain, Sichuan Basin, and YRD are the areas with high concentrations of SO_2 and NO_2. The eastern China, in particular, the YRD area is the most-developed area with dense population, major industry (e.g., coal mining, and coal-fire power plants in surrounding provinces), and heavy traffics, which cause large emissions. Sichuan Basin is also highly-polluted due to large local emissions of air pollutants that are not dispersed efficiently under its special meteorological conditions (e.g., lack of sunny days, featured with cloudy, high RH, low wind speed and also temperature inversion) and complex terrain (the basin is surrounded by mountains that are 1000–3000 m above sea level).

Table 2 summarizes overall performance statistics for daily-average surface concentrations of SO_2 and NO_2, max. 1-h O_3, and daily-average PM_{10}. Compared with concentrations derived based on API in major cities, CMAQ underpredicts both SO_2 and NO_2 concentrations in all 4 months (with NMBs from −12.7% to −51.8% for SO_2 and from −6.5% to −32.0% for NO_2), due mainly to underestimated emissions. Q. Zhang et al. (2009) indicated that emissions in 2006 over China were highly uncertain at individual sites, which would affect the accuracy of the projected 2008 emission used here. Several other possible factors may include the inaccuracies in the simulated meteorology, uncertainties in the calculated dry deposition rates, as well as biases in the estimated observations derived from the API. For example, wind speeds are overpredicted by 40–86% (Cheng et al., in preparation), which may blow too much amount of pollutants out of the domain. For comparison, Wang et al. (2009) reported an NMB of 81.3% for surface NO_2 in China using CMAQ 4.4 at 120 km. Despite small NMBs here, NMEs and RMSEs are large for SO_2 and NO_2, indicating some compensation errors.

Table 2
Model performance of surface chemical concentrations at a 36-km horizontal grid resolution.

Mo.	SO_2						NO_2						Max. 1-h O_3						PM_{10} ($\mu g\ m^{-3}$)					
	Obs	Sim	Corr	RMSE	NMB	NME	Obs	Sim	Corr	RMSE	NMB	NME	Obs	Sim	Corr	RMSE	NMB	NME	Obs	Sim	Corr	RMSE	NMB	NME
Jan.	35.6	17.2	0.1	30.6	−51.8	69.4	26.8	25.0	0.6	15.5	−6.5	47.1	37.9	42.5	0.5	9.3	12.0	16.9	120.7	76.3	0.3	88.8	−36.8	54.9
Apr.	24.6	16.0	−0.02	26.4	−34.9	69.1	20.5	13.9	0.5	16.2	−32.0	61.9	61.3	62.3	0.6	14.9	1.6	17.9	104.0	50.4	0.2	73.4	−51.5	57.6
Jul.	15.3	11.3	0.01	16.3	−25.9	77.3	13.4	10.8	0.4	12.6	−19.7	66.6	43.0	51.1	0.5	19.5	19.3	36.6	84.9	38.9	0.3	57.1	−54.2	57.9
Oct.	23.7	20.7	0.06	26.2	−12.7	68.1	23.3	16.2	0.3	16.2	−30.3	54.0	47.0	47.5	0.7	10.7	1.1	17.1	99.4	69.5	0.4	59.3	−30.1	47.1

Obs – observation, ppb, Sim – simulation, ppb, Corr – correlation coefficient, RMSE – root mean square error, ppb, NMB – normalized mean bias, %, NME – normalized mean error, %.

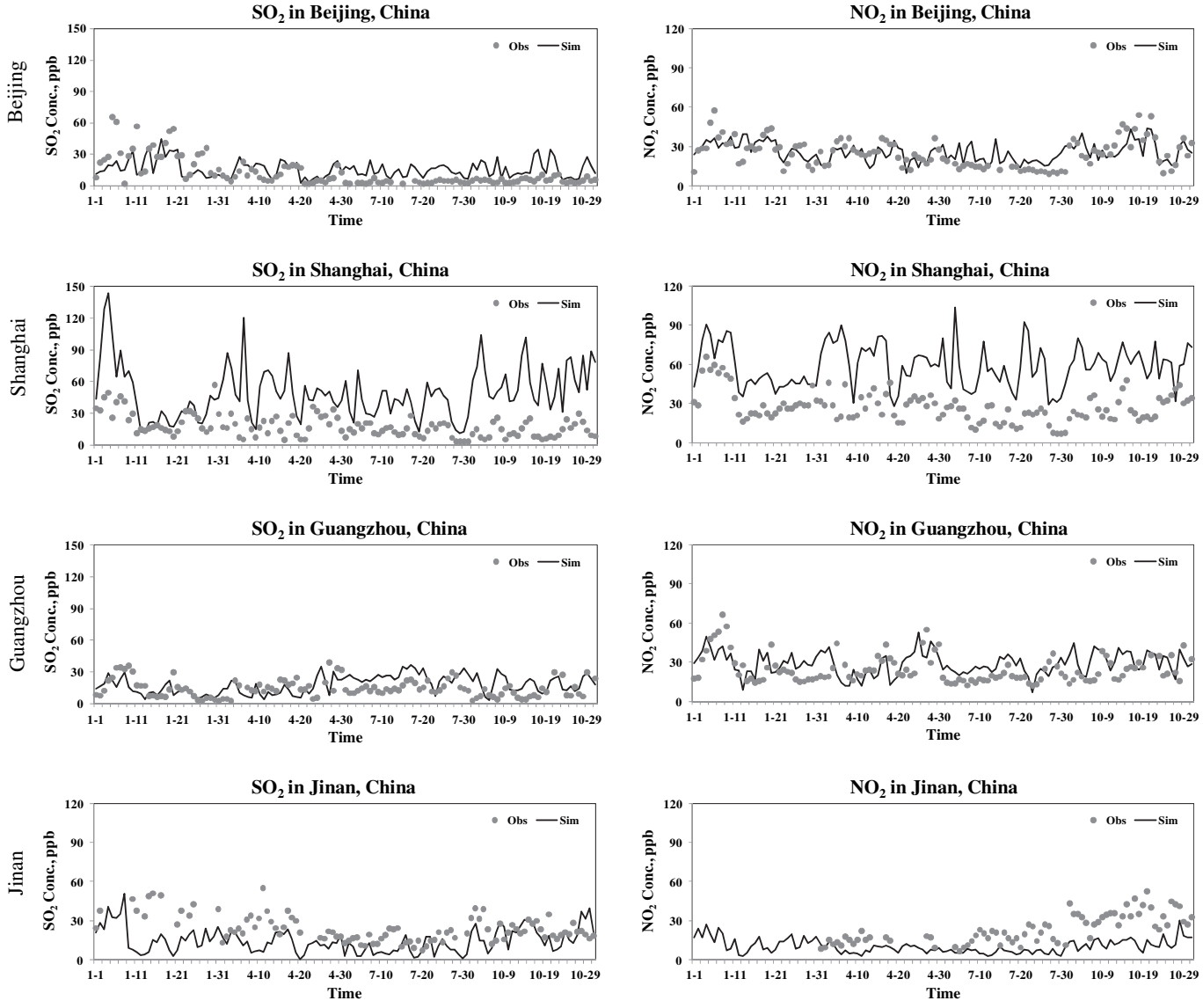

Fig. 2. Temporal variations of SO_2 and NO_2 at four sites (Beijing, Shanghai, Guangzhou, Jinan) in China.

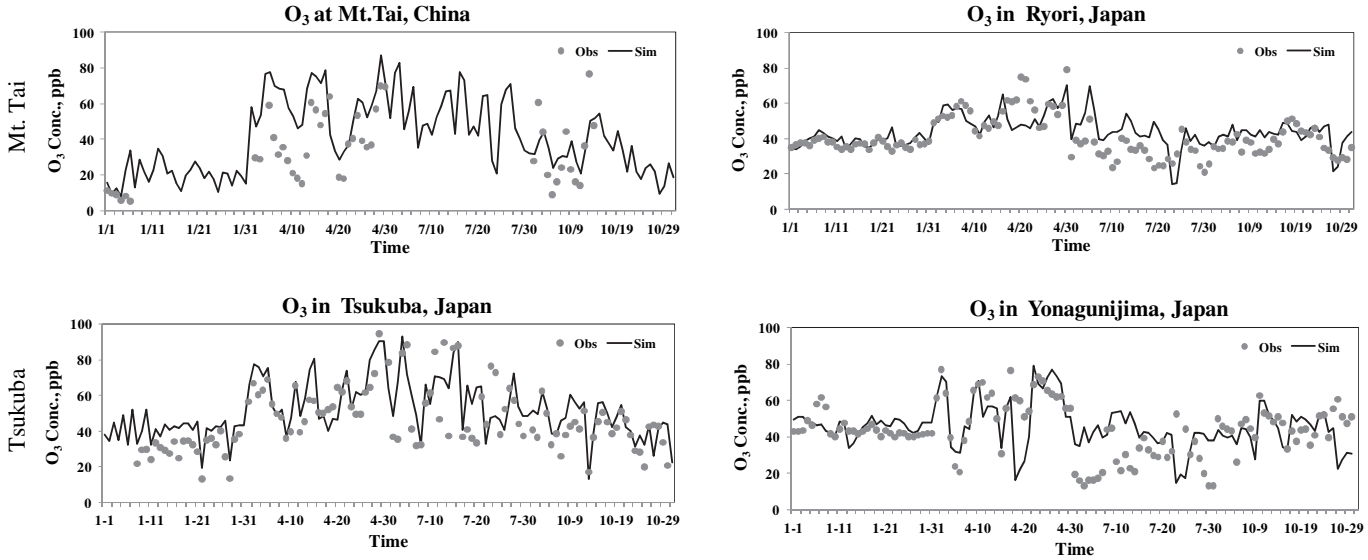

Fig. 3. Temporal variations of O_3 at four sites (Mt. Tai in China and Ryori, Tsukuba, and Yonagunijima in Japan).

The simulated distribution pattern for surface O_3 mixing ratios is different from that of SO_2, NO_2, and PM_{10}. The highest monthly-mean max. 1-h O_3 mixing ratios (up to 107 ppb) occur in Jul. over North China Plain (including Hebei, Shandong, Shanxi, and Henan province), and YRD, due to relatively higher VOC emissions and a strong photochemical production. O_3 mixing ratios over the southern China in Jul. are much lower than those of North China Plain, likely due to the monsoon intrusion of clean air mass from tropical Pacific (Yamaji et al., 2006; Lin et al., 2008). The lowest O_3 mixing ratios in Jul. are found over the Tibetan Plateau mainly due to lack of local sources for O_3 precursors. Compared with Jul., Apr. also has relatively high O_3 mixing ratios of >56 ppb over large areas. This is consistent with the findings of Monks (2000) that the spring surface O_3 maximum occurred widely across mid-latitudes in the Northern Hemisphere, due to relatively high O_3 precursor emissions and the accumulation of O_3 precursors during the winter and sufficiently strong sunlight for photochemical oxidations, high inflow O_3 from boundaries, as well as less precipitation and wet scavenging. Stratospheric–tropospheric exchange might be another factor to the O_3 spring maximum. Jan. has relatively lower O_3 mixing ratios (20–48 ppb) mainly because the production of O_3 is suppressed by the weak solar radiation and low temperatures (Yamaji et al., 2006). High O_3 of 56–64 ppb are found over the Tibetan Plateau in the western China in Jan., due likely in part to a weak or no titration of O_3 because of low NO mixing ratios (<50 ppt) in this region. Other studies reported several other factors such as the downward transport of O_3 from stratosphere (Wang and Li, 1998) or inflow of O_3 and its precursors from the boundary in winter (Yamaji et al., 2006). While CMAQ does not simulate the former process, the boundary conditions generated based on GEOS–CHEM may reflect the impact of inflow to some extent. Despite slightly higher O_3 mixing ratios in Apr. and Jul., the simulated spatial distribution patterns of surface O_3 in this study are similar to those in 2002 simulated by Yamaji et al. (2006). The simulated 1-h O_3 values agree well with limited observations at four sites (90–120 data pairs) with the best agreement in Oct. (an NMB of 1.1%) and the worst in Jul. (an NMB of 19.3%). The discrepancies between simulated and observed O_3 values are likely caused by the uncertainty of precursor emissions such as VOCs and NO_x (e.g., up to ±68% for emissions of VOCs (Q. Zhang et al., 2009)) and simulated meteorological fields.

The simulated PM_{10} also shows the highest concentrations in Jan., with >120 μg m^{-3} (up to 217 μg m^{-3}) over most North China Plain, Sichuan Basin, the east of Hubei province, north of Hunan province, and the Pearl River Delta (PRD) and YRD areas. Those over most regions in the southern China and Northeast Plain are less than 80 μg m^{-3} in winter. Compared with observations, PM_{10} concentrations are well predicted over North China Plain, except some coastal regions (e.g., Qingdao and Yantai in Shandong province) but significantly underpredicted over Northeast Plain, South China, and most areas in the central and western China, which leads to a domain-wide NMB of −36.8% in Jan. Simulated PM_{10} concentrations of >120 μg m^{-3} (up to 185 μg m^{-3}) are also found in Oct., but over a smaller area covering Beijing, Shanghai, and most areas of the Hebei, Henan, and Shandong provinces in Oct. than in Jan. Regional haze, which often occurred in fall and winter (e.g., Sept. 30–Oct. 6, 2008), partially contributes to the high observed PM_{10} concentrations in Oct. Compared with observations, the model underpredicts PM_{10} concentrations with an NMB of −30.1%. Although observed PM_{10} concentrations remained high in Apr., the simulated PM_{10} concentrations in Apr. are much lower than those in Jan. and Oct., with PM_{10} concentrations of 100–128 μg m^{-3} occurring at only a few sites in Hebei province. Simulated PM_{10} is significantly underpredicted with a domain-wide NMB of −51.5%. Lack of a dust emission module in CMAQ4.7 is one possible reason for this underprediction, although some coarse-mode PM species (i.e., SO_4^{2-}, NO_3^-, NH_4^+, Na^+, and Cl^-) are simulated in CMAQ v4.7 through gas/particle mass transfer. The lowest PM_{10} concentrations occur in Jul., due to heavy precipitation and other meteorology conditions such as stronger convective mixing, and higher PBL height than Jan. The simulated PM_{10} concentrations in almost all cities located outside the North China Plain are much lower than observations, resulting in a significant underprediction over the entire domain in Jul., with the largest NMB of −54.2% among all four months. For comparison, Wang et al. (2009) reported up to 85.6% underprediction for PM_{10} over China using CMAQ 4.4 at a grid resolution of 120 km, which is

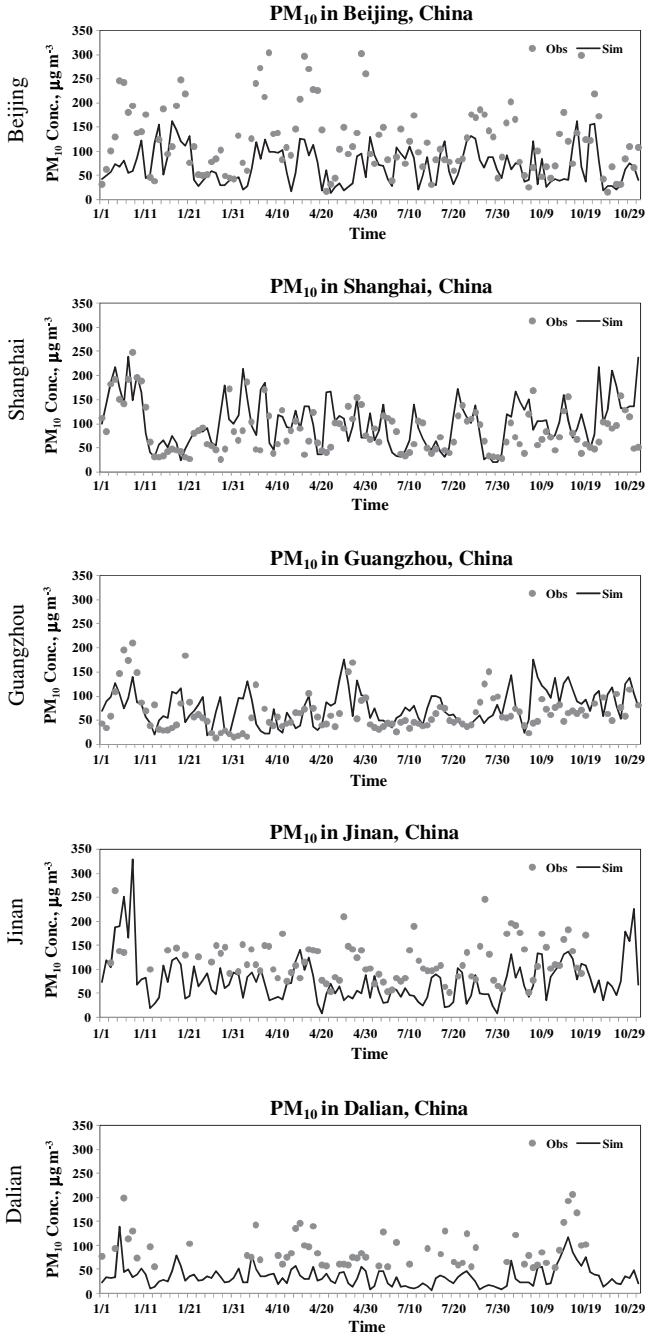

Fig. 4. Temporal variations of PM_{10} at five sites (Beijing, Shanghai, Guangzhou, Jinan, and Dalian) in China.

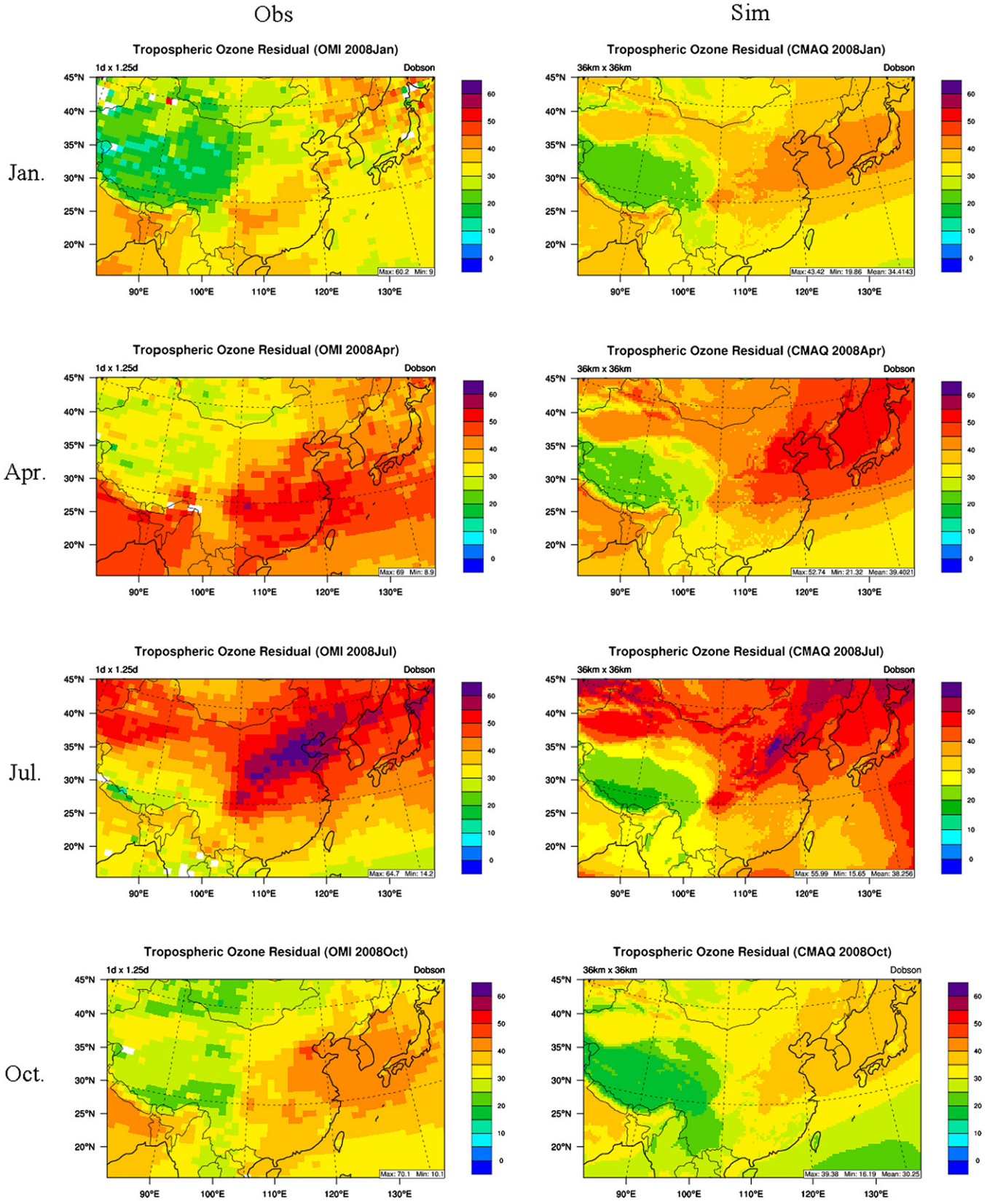

Fig. 5. Spatial distributions of monthly-mean TOR from observations (left) and simulations (right) in Jan., Apr., Jul. and Oct. 2008.

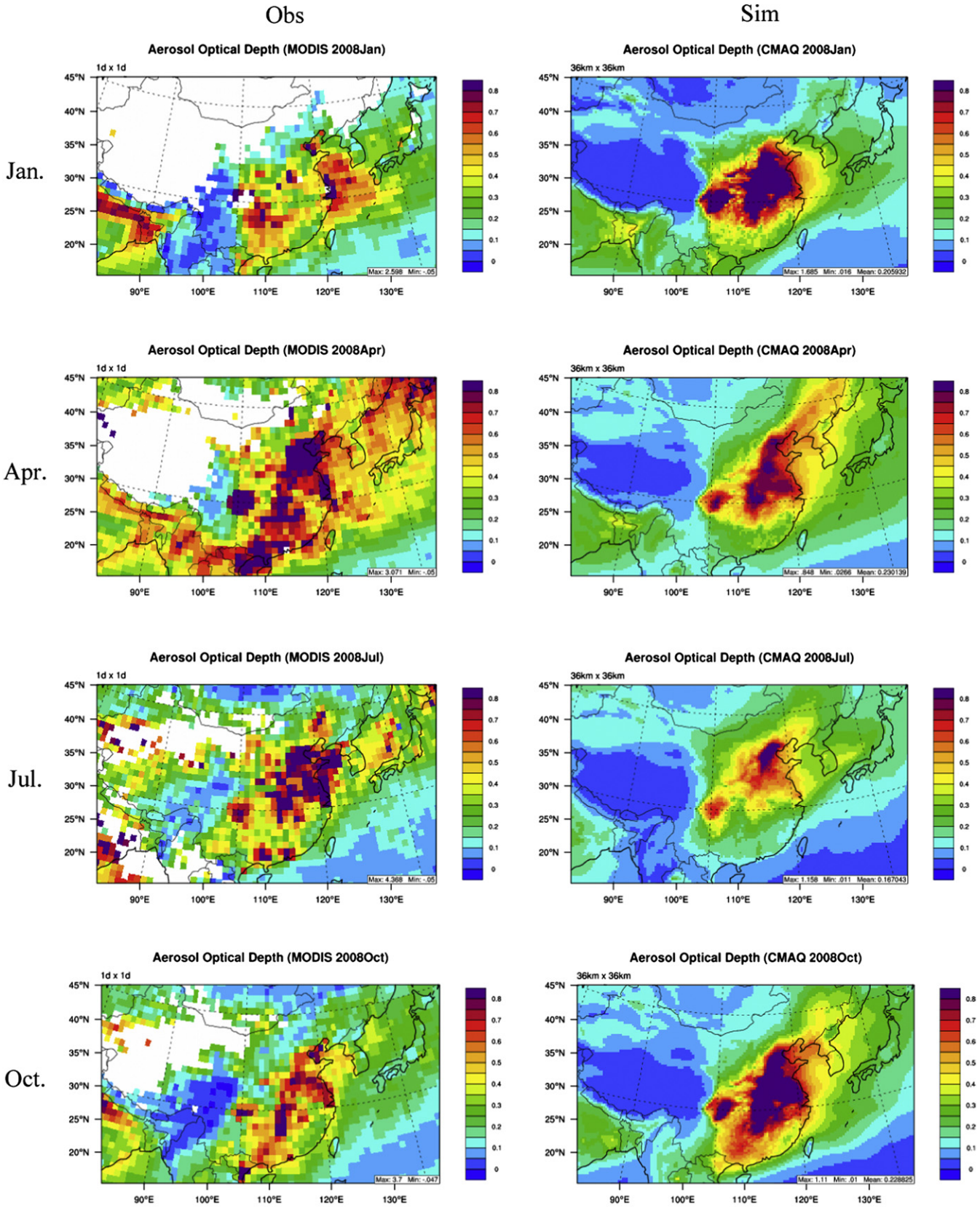

Fig. 6. Spatial distributions of monthly-mean AODs from observations (left) and simulations (right) in Jan., Apr., Jul. and Oct. 2008.

worse than this study. Factors contributing to the underpredictions may include underestimated emissions of primary PM species such as black carbon and organic carbon and emissions of the precursors for secondary PM such as SO_2 and NO_2, as well as the emissions of NH_3 (e.g., NH_3 emissions used here for the PRD areas are ~20% lower than the latest emission estimates by J.-Y. Zheng, South China University of technology, personal communications, 2009), in addition to inaccurate meteorological predictions (e.g., overpredicted wind speeds by about 40% in Jul.). The primary PM_{10} emission rates larger than 100 g s^{-1} are concentrated over the North China Plain, Sichuan Basin, and YRD and PRD in all months while those in the central and western China are smaller than 8.0 g s^{-1}. The high levels of PM_{10} occur over the source regions in all months with 40–95.4% primary PM_{10}, indicating a large influence of primary PM_{10} over these regions. However, the seasonal variations and magnitude of emissions of primary PM_{10} are not always consistent with those of the simulated PM_{10} concentrations because of the formation of the secondary PM and the influence of meteorology in the accumulation and transport of PM_{10}.

3.1.2. Temporal variation

Figs. 2–4 show the observed and simulated temporal variations of daily-average SO_2 and NO_2 at four urban sites (i.e., Beijing, Shanghai, Guangzhou, Jinan in China), max. 1-h O_3 at three rural sites (i.e., Ryori, Tsukuba, and Yonagunijima in Japan) and one mountain site (i.e., Mt. Tai in China), and daily-average PM_{10} at five urban sites (i.e., Beijing, Shanghai, Guangzhou, Jinan, and Dalian in China). CMAQ reproduces SO_2 concentrations well for all months at Guangzhou, in Jan. and Apr. at Beijing, and in Jul. and Oct. at Jinan but overpredicts those in all months at Shanghai and in Jul. and Oct. at Beijing and underpredicts those in Jan. and Apr. at Jinan and all months at other sites (Figures not shown). CMAQ reproduces the mixing ratios of NO_2 in terms of magnitude and variation trends at Beijing and Guangzhou, but overpredicts at Shanghai and underpredicts at Jinan on most days. Temporal variations of O_3 mixing ratios at all sites in Japan are reproduced well on most days, except slight overpredictions in late Apr. and Jul. at Tsukuba and Yonagunijima. At Mt. Tai, CMAQ well captures the O_3 mixing ratios of the first several days in Jan., but overpredicts those in Apr., either overpredicts or underpredicts those in Oct. Compared with observations, the PM_{10} concentrations simulated at Beijing, Jinan, and Dalian are underpredicted in all four months, particularly at Beijing. However, good performance is found at Shanghai and Guangzhou.

3.2. Column variables

Figs. S-2, S-3, 5 and 6 compare simulated spatial distribution of monthly-mean column abundance of CO and NO_2, TOR, and AOD, respectively, with observations from satellite data. Compared with satellite data, column CO is significantly underpredicted in Apr. with an NMB of −29.3% and NME of 31.1%, and best predicted in Oct. with an NMB of −1.0% and NME of 14.5% (see Table 3). In Jan. and Oct., underpredictions occur over the western and northern China as well as the oceanic area off the east coast of China and compensate overpredictions in the eastern and southern China, resulting in small NMBs. These biases may be caused by the uncertainties in the CO emissions and boundary conditions used (Y. Zhang et al., 2009).

CMAQ reproduces well the spatial distribution pattern and seasonality of column NO_2 with high correlation coefficients of 0.7–0.9. Higher column NO_2 is found over the eastern China including Beijing, Hebei, Henan, Shandong, YRD and PRD than the remaining areas in all months. Observed and simulated column NO_2 concentrations are maximum in Jan., followed by Oct., Apr., and Jul. The high winter values are likely resulted from a combined effect of decreased loss of NO_2 via its reaction with OH, reduced

Table 3
Model performance of column variables at a 36-km horizontal grid resolution.

Mo.	CO						NO_2						TOR						AOD					
	Obs	Sim	Corr	RMSE	NMB	NME	Obs	Sim	Corr	RMSE	NMB	NME	Obs	Sim	Corr	RMSE	NMB	NME	Obs	Sim	Corr	RMSE	NMB	NME
Jan.	19.6	19.1	0.6	5.8	−3.0	20.9	23.4	32.8	0.9	27.0	40.4	58.1	30.7	34.4	0.6	6.4	12.1	16.1	0.27	0.26	0.6	0.2	−4.0	45.7
Apr.	23.9	16.9	0.8	8.0	−29.3	31.1	20.1	21.4	0.8	16.4	6.3	41.5	40.6	39.4	0.3	8.7	−3.0	19.7	0.45	0.26	0.6	0.3	−43.0	44.9
Jul.	16.8	15.4	0.5	5.9	−8.4	29.7	17.4	15.4	0.7	15.4	−11.5	46.3	42.1	38.3	0.7	7.2	−9.1	14.2	0.32	0.17	0.6	0.2	−45.8	51.4
Oct.	18.4	18.2	0.8	3.5	−1.0	14.5	17.8	24.1	0.8	22.9	35.4	54.6	33.8	30.3	0.7	5.7	−10.6	15.0	0.25	0.24	0.7	0.1	−1.7	41.9

1. Obs – observation, Sim – simulation, Corr – correlation coefficient, RMSE – root mean square error, NMB – normalized mean bias, %, NME – normalized mean error, %, TOR – tropospheric ozone residual, AOD – aerosol optical depth.
2. The unit for Obs, Sim, and RMSE are in 1×10^{17} molecules cm^{-2} for CO, 1×10^{15} molecules cm^{-2} for NO_2, and Dobson for TOR.

Table 4
Model performance at horizontal grid resolutions of 36- and 12-km over the eastern China.

Surface chemical concentrations at 12- and 36-km																								
Mo.		SO_2						NO_2						1-h O_3						PM_{10}					
		Obs	Sim	Corr	RMSE	NMB	NME	Obs	Sim	Corr	RMSE	NMB	NME	Obs	Sim	Corr	RMSE	NMB	NME	Obs	Sim	Corr	RMSE	NMB	NME
Jan.	12-km	34.8	27.8	0.09	40.1	−20.2	76.6	29.3	36.8	0.5	28.5	25.5	70.2	41.1	45.9	0.3	11.2	11.6	18.1	119.9	103.6	0.3	78.7	−13.6	47.6
	36-km	34.8	15.9	0.10	30.9	−54.4	70.7	29.3	28.3	0.5	16.6	−3.4	47.7	41.1	44.8	0.3	10.8	9.1	17.0	119.9	84.7	0.4	79.8	−29.4	48.4
Apr.	12-km	24.7	27.7	−0.07	40.2	12.2	94.1	21.1	22.0	0.3	22.9	4.5	70.9	62.7	64.1	0.6	17.3	2.4	20.9	103.9	72.3	0.2	63.4	−30.4	47.7
	36-km	24.7	16.3	−0.03	26.9	−33.8	69.8	21.1	14.6	0.4	16.7	−31.0	62.1	62.7	64.6	0.6	18.3	3.2	21.5	103.9	58.7	0.2	65.8	−43.6	51.3
Jul.	12-km	15.3	21.2	−0.03	28.8	38.7	115.6	13.7	18.8	0.3	19.5	37.5	83.2	30.8	41.0	−0.4	22.9	33.0	58.8	86.1	60.0	0.3	50.8	−30.3	47.8
	36-km	15.3	11.4	0.01	16.6	−25.6	78.7	13.7	11.1	0.4	12.9	−18.7	67.2	30.8	40.0	−0.5	24.9	30.0	62.7	86.1	44.7	0.3	54.3	−48.1	52.8
Oct.	12-km	24.2	37.5	−0.06	53.1	54.6	114.3	23.9	25.6	0.3	21.9	6.8	54.3	54.3	48.2	0.7	15.4	−11.2	20.4	103.4	101.3	0.3	62.6	−2.1	42.9
	36-km	24.2	20.9	0.05	26.7	−13.5	68.6	23.9	16.6	0.3	16.6	−30.5	54.4	54.3	48.9	0.8	13.2	−9.9	17.5	103.4	79.6	0.3	56.5	−23.1	42.3
Column variables at 12- and 36-km																									
Mo.		CO						NO_2						TOR						AOD					
		Obs	Sim	Corr	RMSE	NMB	NME	Obs	Sim	Corr	RMSE	NMB	NME	Obs	Sim	Corr	RMSE	NMB	NME	Obs	Sim	Corr	RMSE	NMB	NME
Jan.	12-km	22.9	24.2	0.2	7.4	5.2	22.8	69.1	97.8	0.8	61.3	41.6	62.2	33.2	37.3	0.1	6.1	12.6	15.1	0.38	0.44	0.4	0.3	14.3	49.1
	36-km	22.9	24.6	0.3	7.5	7.5	22.7	68.7	93.3	0.8	50.7	35.9	52.9	33.2	37.2	0.1	6.0	12.2	14.9	0.38	0.46	0.5	0.3	20.6	51.6
Apr.	12-km	25.9	20.3	0.3	7.4	−21.2	26.9	44.6	55.2	0.7	37.5	23.8	54.8	45.0	42.6	−0.1	8.9	−5.5	17.8	0.61	0.43	0.5	0.3	−29.7	33.1
	36-km	25.9	20.6	0.3	7.3	−20.2	26.4	44.1	49.4	0.8	30.3	12.0	44.6	44.9	42.8	−0.1	8.9	−4.8	18.0	0.61	0.43	0.5	0.3	−28.9	32.3
Jul.	12-km	20.7	19.2	0.5	4.2	−7.2	16.2	37.1	38.2	0.6	33.4	2.9	51.4	47.9	40.3	0.9	8.7	−15.9	16.2	0.49	0.33	0.7	0.3	−32.5	38.8
	36-km	20.7	19.6	0.5	4.1	−5.2	15.2	36.4	34.8	0.6	28.3	−4.4	44.9	47.9	41.0	0.9	8.1	−14.5	15.0	0.49	0.33	0.7	0.3	−33.4	38.8
Oct.	12-km	21.5	22.7	0.7	3.7	5.3	12.7	41.7	68.0	0.7	52.2	63.1	76.4	37.8	33.2	0.7	5.3	−12.0	12.4	0.39	0.49	0.8	0.2	25.5	35.7
	36-km	21.5	22.9	0.7	4.0	6.55	13.8	40.9	60.6	0.8	43.9	48.1	62.5	37.7	33.5	0.7	5.1	−11.4	11.9	0.39	0.50	0.8	0.2	29.6	39.1

1. Obs – observation, ppb, Sim – simulation, ppb, Corr – correlation coefficient, RMSE – root mean square error, ppb, NMB – normalized mean bias, %, NME – normalized mean error, %, TOR – tropospheric ozone residual, AOD – aerosol optical depth.
2. The unit for Obs, Sim, and RMSE are in 1×10^{17} molecules cm^{-2} for CO, 1×10^{15} molecules cm^{-2} for NO_2, and Dobson for TOR.

vertical transport from the PBL to higher altitudes, and slightly increased emissions (Wang et al., 2009). The lower column NO_2 in Apr. and Jul. may be related to stronger photochemical reactions that convert it into other reactive nitrogen species during late spring and summer. Comparison with satellite data indicates an underprediction with an NMB of −11.5% in Jul. but overpredictions with NMBs of 6.3–40.4% in other months. For comparison, Han et al. (2009) reported >50% underprediction over North China and as much as 46% overprediction over South Korea for their simulated column NO_2 using CMAQ. Uncertainties in emission inventories of NO_x and related species such as isoprene may contribute the model biases.

As shown in Fig. 5, the observed TOR is the highest in the eastern China due to enhanced pollution and the lowest in the Tibetan Plateau that is the highest landmass in the world, with an average height of >4-km above sea level. The low observed TOR in the Tibetan Plateau can be attributed to two main factors including the thinness of the air column that can lead to ~2.5% (~10 Dobson Unit (DU)) reduction in total column O_3 and the large-scale uplift and descent of isentropic surfaces during the monsoon anticyclone circulation that shifted the vertical profiles of O_3 (Tian et al., 2008). Simulated and observed TOR in Jan., Apr., and Oct. are comparable, but all with overpredictions in the northeastern China and underpredictions over the southern China and Tibetan Plateau. The spatial distribution of observed TOR in Jul. is reproduced well but underpredictions occur over Hebei, Shandong, and Shanxi where the highest observations in Jul. occurred and over Tibetan Plateau. Domain-wide TOR is overpredicted in Jan. with an NMB of 12.1% and NME of 16.1%, and slightly underpredicted in other months, with NMBs of −10.6% to −3.0% and NMEs of 14.2–19.7%. The biases of TOR are strongly related to the uncertainties in the upper-layer boundary conditions of O_3 generated from GEOS–CHEM. Boundary O_3 mixing ratios from layers 10 to 14 used here are 41.0, 46.4, 58.6, and 36.5 ppb in Jan., Apr., Jul., and Oct., respectively. The uncertainty associated with the satellite retrieval algorithms may also influence the accuracy of observed TORs.

Compared with satellite AODs (Fig. 6), the model captures the high AODs over the North China Plain, YRD and PRD areas in the eastern China and Sichuan Basin in all four months, although it significantly overpredicts in Jan. and Oct., and underpredicts in Apr. While observed AODs are the highest in Apr., followed by Jul., Oct., and Jan., the simulated AODs are the highest in Jan., followed by Oct., Apr., and Jul. Domain-wide AODs are slightly underpredicted in Jan. and Oct., respectively. In Apr., simulated AODs in the north of YRD are reasonably good, underpredictions occur over the southern China, Japan, and Pacific ocean with a domain-wide NMB of −43.0% and NME of 44.9%. Underpredictions also occur throughout the whole domain in Jul. with an NMB of −45.8% and NME of 51.4%. The discrepancies between simulated and observed AODs might be caused by several factors, such as the underpredictions of PM concentrations as shown in Table 2, uncertainties in the boundary conditions used, and calculated AODs based on CMAQ PM simulations using an empirical equation (Wang et al., 2009; Y. Zhang et al., 2009).

3.3. Sensitivity of model predictions to horizontal grid resolution

Different grid resolution could influence modeling simulation performance due to a more detailed representation of emissions, land use, meteorological and chemical processes at finer grid resolutions. Some studies have shown that atmospheric modeling at finer resolutions may help improve the model performance (Lin et al., 2008), while some show that chemistry did not show linear relationship with horizontal grid resolution and the model did not always perform well at finer grid resolutions (e.g., Jang, 1995; Queen and Zhang, 2008; Wu et al., 2008). In addition, horizontal grid resolution can affect O_3 responses to changes in precursor emissions, with increased nonlinearity of O_3 production with respect to NO_x emissions at a finer grid scale (Cohan et al., 2006).

The spatial distribution patterns are almost identical between 12- and 36-km grid resolutions for all surface and column variables, although there are some differences over the areas with relatively higher pollutant concentrations, indicating that the model simulation at 12-km captures more detailed information over urban areas due to more detailed terrain and emissions (see Fig. S-4 and analysis in the Supplementary data). Table 4 shows the performance statistic over the eastern China at 12- and 36-km. For surface concentrations of NO_2 and PM_{10}, CMAQ performs better at 12-km than those at 36-km in all four months because of their higher concentrations at 12-km, with differences in NMBs > 10%. SO_2 concentrations at 12-km are closer to observations compared with those at 36-km in Jan. and Apr., but deviate more from observations in Jul. and Oct. at 36-km. Model performance for 1-h O_3 varies slightly at 12- and 36-km, with <3% difference NMBs. The model performance in terms of reproducing column variables at 12-km is slightly better than that at 36-km for column CO in Jan. and Oct., column NO_2 in Jul., and AODs in Jan., Jul., and Oct. but slightly worse in other months for those variables and for TOR for all months. The differences of model performance for domain-wide column variables at two grid resolutions are overall quite small, with less than 8% difference in NMBs except column NO_2 in Apr. and Oct.

4. Conclusions

CMAQ v4.7 is applied to simulate such pollution and its seasonality over East Asia in Jan., Apr., Jul., and Oct. 2008 and the results are evaluated with available surface and satellite data. Both predicted surface species (i.e., SO_2, NO_2, max. 1-h O_3, and PM_{10}) and column variables (e.g., column CO and NO_2, TOR, and AOD) show strong seasonality and spatial variations. The simulated concentrations of SO_2, NO_2, and PM_{10} in Jan. are the highest throughout the year, followed by Oct., Apr., and Jul., whereas the simulated mixing ratios of O_3 are the highest in Jul., followed by Apr., Oct., and Jan. While the model captures well the observed seasonal variations of PM_{10} concentrations, the model's capability in reproducing seasonal variations of surface concentrations of SO_2, NO_2, and O_3 cannot be accurately evaluated because of limited publically-available observational data. The simulated column CO, NO_2, and AODs are the highest in Jan., followed by Oct., Apr., and Jul., whereas the simulated TORs are the highest in Jul., followed by Apr., Jan., and Oct. Compared with satellite observations, the model captures well the seasonality of column NO_2 and AODs, but fails to reproduce those of column CO and TORs. High surface max. 1-h O_3 and TOR are found in Jul. and Apr. due to strong photochemical reactions for all layers and high boundary concentrations for upper layers, while other surface or column variables tend to be higher in Jan. and Oct. Most pollutants show very high concentrations over the eastern China surrounding Beijing, YRD, and PRD due to large emissions from dense population, rapid economic development, heavy traffic, and high energy consumption as well as stagnant meteorological conditions and complex terrain.

For surface species, SO_2, NO_2, and PM_{10} are all significantly underpredicted in all four months, with NMBs up to −51.8%, −32.0%, and −54.2%, respectively. These large discrepancies might be caused by several factors such as uncertainties in the emissions and simulated meteorology. The mixing ratios of max. 1-h O_3 in Jan. and Jul. are overpredicted with NMBs about 12.0% and 19.3%, respectively. Most simulated column variables could generally capture the spatial distribution patterns with high values over the eastern China and relatively lower values over the central and western China. Large underpredictions, however, are found for

column CO in Apr., TOR in Jul., and AODs in both Apr. and Jul. over the northeastern China, while overprediction occur in column CO in Oct., column NO_2 in Jan. and Oct., AODs in Jan. and Oct. over the eastern China. The discrepancy of column variables may be related to the boundary conditions which affect their vertical profiles.

The spatial distribution patterns of surface concentrations and column variables at 12-km are overall similar to those at 36-km, but providing more detailed information over higher polluted areas, although it does not always lead to better model performance. The surface concentrations are more sensitive to grid resolution with relatively larger discrepancies (>5%) occurring over the complex terrain such as the mountain and coastal areas, mainly because different surface characteristics may result in different local circulation and meteorological conditions that in turn affect transport and chemistry of pollutants.

The model evaluation in this study indicates an overall acceptable performance especially for surface O_3 and column variables. The major reasons for the model biases include uncertainties in emissions and upper-layer boundary conditions (e.g., TORs) and model deficiencies (i.e., neglecting some coarse-mode species such as mineral dust). Other possible reasons include uncertainties simulated meteorology (such as the limitation of the use of a coarse grid resolution in capturing fine scale meteorological phenomena (Wang et al., 2009)) and uncertainties in the observations from API and satellite data.

Acknowledgements

The authors thank Xin-Yu Wen and Yao-Sheng Chen at North Carolina State University for post-processing and analysis of satellite data; Peng-Ju Xu at Shandong University for providing the O_3 monitoring data at Mt Tai. The O_3 data at 3 sites in Japan were provided by World Data Center for Greenhouse Gases. This work was funded by the U.S. NSF Career Award No. Atm-0348819, the U.S. EPA, and Shandong University in China. The meteorological simulations were funded by China Scholarship Council at Shandong University in China and the U.S. NSF Career Award No. Atm-0348819 at NCSU.

Appendix. Supplementary data

Supplementary data associated with this article can be found, in the online version, at doi:10.1016/j.atmosenv.2010.03.035.

References

An, X., Zhu, T., Wang, Z., Li, C., Wang, Y., 2007. A modeling analysis of a heavy air pollution episode occurred in Beijing. Atmospheric Chemistry and Physics 7, 3101–3114.

Byun, D.W., Schere, K.L., 2006. Review of the governing equations, computational algorithms, and other components of the Models-3 Community Multiscale Air Quality (CMAQ) Modeling System. Applied Mechanics Reviews 59, 51–77.

Chen, D., Cheng, S., Liu, L., Chen, T., Guo, X., 2007. An integrated MM5–CMAQ modeling approach for assessing trans-boundary PM_{10} contribution to the host city of 2008 Olympic summer games – Beijing, China. Atmospheric Environment 41, 1237–1250.

Cheng, S.-H., Zhang, Y., Chen, Y.-S., Wang, W.-X., Gilliam, R.C., Pleim, J. Application of MM5 in China: Model evaluation, seasonal variations, and sensitivity to horizontal grid resolutions. Atmospheric Environment, in preparation.

Cohan, D.S., Hu, Y., Russell, A.G., 2006. Dependence of ozone sensitivity analysis on grid resolution. Atmospheric Environment 40, 126–135.

Han, K.M., Song, C.H., Ahn, H.J., Park, R.S., Woo, J.H., Lee, C.K., Richter, A., Burrows, J.P., Kim, J.Y., Hong, J.H., 2009. Investigation of NO_x emissions and NO_x-related chemistry in East Asia using CMAQ-predicted and GOME-derived NO_2 columns. Atmospheric Chemistry and Physics 9, 1017–1036.

Hao, J.-M., He, K.-B., Duan, L., Li, J.-H., Wang, L.-T., 2007. Air pollution and its control in China. Frontiers of Environmental Science and Engineering in China 1, 129–142.

Jang, C.J., 1995. Sensitivity of ozone to model grid resolution – II, detailed process analysis for ozone chemistry. Atmospheric Environment 29, 3101–3114.

Jiang, D.-H., Zhang, Y., Hu, X., Zeng, Y., Tan, J.-G., Shao, D.-M., 2004. Progress in developing an ANN model for air pollution index forecasting. Atmospheric Environment 28, 7055–7064.

Lin, M., Holloway, T., Oki, T., Streets, D.G., Richter, A., 2008. Mechanisms controlling surface ozone over East Asia: a multiscale study coupling regional and global chemical transport models. Atmospheric Chemistry and Physics Discussions 8, 20239–20281.

Liu, L., Sundet, J.K., Liu, Y., Berntsen, T.K., Isaksen, I.S., 2007. A study of tropospheric ozone over China with a 3-D global CTM model. Terrestrial, Atmospheric and Oceanic Sciences 18, 515–545.

Monks, P.S., 2000. A review of the observations and origins of the spring ozone maximum. Atmospheric Environment 34, 3545–3561.

Queen, A., Zhang, Y., 2008. Examining the sensitivity of MM5–CMAQ predictions to explicit microphysics schemes and horizontal grid resolutions, part III—the impact of horizontal grid resolution. Atmospheric Environment 42, 3869–3881.

Song, C.H., Park, M.E., Lee, K.H., Ahn, H.J., Lee, Y., Kim, J.Y., Han, K.M., Kim, J., Ghim, Y.S., Kim, Y.J., 2008. An investigation into seasonal and regional aerosol characteristics in East Asia using model-predicted and remotely-sensed aerosol properties. Atmospheric Chemistry and Physics 8, 6627–6654.

Streets, D.G., Fu, J.S., Jang, C.J., Hao, J.-M., He, K.-B., Tang, X.-Y., Zhang, Y.-H., Wang, Z.-F., Li, Z.-P., Zhang, Q., Wang, L.-T., Wang, B.-Y., Yu, C., 2007. Air quality during the 2008 Beijing Olympic Games. Atmospheric Environment 41, 480–492.

Streets, D.G., Zhang, Q., Wang, L.-T., He, K.-B., Hao, J.-M., Wu, Y., Tang, Y.-H., Carmichael, G.R., 2006. Revisiting China's CO emissions after the Transport and Chemical Evolution over the Pacific (TRACE-P) mission: synthesis of inventories, atmospheric modeling, and observations. Journal of Geophysical Research 111 (D14306). doi:10.1029/2006JD007118.

Tian, W.-S., Chipperfield, M., Huang, Q., 2008. Effects of the Tibetan Plateau on total column ozone distribution. Tellus 60B, 622–635.

Tie, X.-X., Brasseur, G.P., Zhao, C.-S., Granier, C., Massie, S., Qin, Y., Wang, P.-C., Wang, G.-L., Yang, P.-C., Richter, A., 2006. Chemical characterization of air pollution in Eastern China and the Eastern United States. Atmospheric Environment 40, 2607–2625.

Wang, X.-H., Li, X.-S., 1998. A numerical study of the variations and distribution of tropospheric ozone and its precursors over China. Acta Meteorologica Sinica 56, 333–348.

Wang, K., Zhang, Y., Jang, C.J., Phillips, S., Wang, B.-Y., 2009. Modeling study of intercontinental air pollution transport over the trans-Pacific region in 2001 using the Community Multiscale Air Quality (CMAQ) modeling system. Journal of Geophysical Research 114 (D04307). doi:10.1029/2008JD010807.

Wu, S.-Y., Krishnan, S., Zhang, Y., Aneja, V., 2008. Modeling atmospheric transport and fate of ammonia in North Carolina, part I. Evaluation of meteorological and chemical predictions. Atmospheric Environment 42, 3419–3436.

Xu, J., Zhang, Y.-H., Fu, J.S., Zheng, S.-Q., Wang, W., 2008. Process analysis of typical summertime ozone episodes over the Beijing area. Science of the Total Environment 399, 147–157.

Yamaji, K., Ohara, T., Uno, I., Tanimoto, H., Kurokawa, J., Akimoto, H., 2006. Analysis of the seasonal variation of ozone in the boundary layer in East Asia using the Community Multi-scale Air Quality model: what controls surface ozone levels over Japan? Atmospheric Environment 40, 1856–1868.

Zhang, Q., Streets, D.G., He, K.-B., Klimont, Z., 2007a. Major components of China's anthropogenic primary particulate emissions. Environmental Research Letters 2 (045027). doi:10.1088/1748-9326/2/4/045027.

Zhang, Q., Streets, D.G., He, K.-B., Wang, Y.-X., Richter, A., Burrows, J.P., Uno, I., Jang, C.J., Chen, D., Yao, Z.L., Lei, Y., 2007b. NO_x emission trends for China, 1995–2004: the view from the ground and the view from space. Journal of Geophysical Research 112 (D22306). doi:10.1029/2007JD008684.

Zhang, Q., Streets, D.G., Carmichael, G.R., He, K.-B., Huo, H., Kannari, A., Klimont, Z., Park, I.S., Reddy, S., Fu, J.S., Chen, D., Duan, L., Lei, Y., Wang, L.-T., Yao, Z.-L., 2009. Asian emissions in 2006 for the NASA INTEX-B mission. Atmospheric Chemistry and Physics Discussions 9, 4081–4139.

Zhang, Y., Vijayaraghavan, K., Wen, X.-Y., Snell, H.E., Jacobson, M.Z., 2009. Probing into regional O_3 and PM pollution in the U.S., part I. A 1-year CMAQ simulation and evaluation using surface and satellite data. Journal of Geophysical Research 114, D22304. doi:10.1029/2009JD011898.